# Understanding High-Speed Aeroelastic Stability of a Gimballed Proprotor

Akinola Akinwale* and Anubhav Datta†
*University of Maryland, College Park, Maryland 20742*

https://doi.org/10.2514/1.C037994

**A 4.75-ft-diameter dynamically scaled proprotor was tested on a semispan wing pylon in airplane mode up to high speeds of 200 kt. Aeroelastic stability data was acquired at two wind tunnels: Navy Carderock tunnel and the University of Maryland Glenn L. Martin tunnel, and for two hub configurations: gimballed and gimbal locked. The data consisted of frequency and damping of beam, chord, and torsion modes of the coupled rotor–wing-pylon system at a Froude-scale rpm of 1050. The eigenvalues were extracted with moving-block and Prony methods and were compared. The tests shed light on the nature of roots in high-speed tiltrotor flight. The key conclusions were the following: 1) the beam and chord damping for the gimballed rotor remained low, around 1–2%; 2) torsion damping was higher, around 3–6%; 3) the gimbal-locked condition increased chord and torsion damping significantly and also changed their trends with speed; 4) the model remained flutter-free up to 200 kt, which is equivalent to 458 kt in full scale; and 5) moving block and Prony are methods equally effective for extracting damping from time-series data for these test conditions.**



## Nomenclature

| | | |
|---|---|---|
| $EI$ | = | bending stiffness, N · m$^2$ |
| $f$ | = | scaling factor |
| $GJ$ | = | torsional stiffness, N · m$^2$ |
| $\delta_3$ | = | pitch–flap coupling angle |
| $\zeta$ | = | damping ratio |
| $\theta_{1c}$ | = | longitudinal cyclic pitch angle |
| $\theta_{1s}$ | = | lateral cyclic pitch angle |
| $\theta_{75}$ | = | collective pitch angle at 75% radius |
| $\nu_b$ | = | rotating flap frequency |
| $\nu_\zeta$ | = | rotating lag frequency, /rev |
| $\nu_\theta$ | = | rotating torsional frequency, /rev |
| $\omega_b$ | = | beam damped frequency, Hz |
| $\omega_c$ | = | chord damped frequency, Hz |
| $\omega_n$ | = | natural frequency, rad/s |
| $\omega_t$ | = | torsion damped frequency, Hz |

## I. Introduction

A 4.75-ft-diameter dynamically scaled proprotor was tested in airplane mode, reaching unprecedented speeds of up to 200 kt. The model was perturbed using high-bandwidth electric actuators and the rotor–wing-pylon damping were measured in beam, chord, and torsion. The beam mode is the first out-of-plane bending mode; chord, the first in-plane bending mode; and torsion, the second out-of-plane bending mode. Data was acquired on a gimballed hub (baseline) as well as a gimbal- locked (stiff in-plane hingeless) hub. The objectives of this paper are to describe the test, analyze the stability characteristics measured at high speed, and document the key insights obtained from the measurements.

Enabling higher speeds of tiltrotors are a subject of considerable current interest. A vision for the future is 450-kt flutter-free cruise, nearly twice as high as current aircraft. Three experimental facilities have reported ongoing research in the United States: the NASA Ames Research Center Tiltrotor Test Rig (TTR) [1,2], the University of Maryland Tiltrotor Rig (MTR) [3–8], and the U.S. Army/NASA Tiltrotor Aeroelastic Stability Testbed (TRAST) [9,10]. The TTR is a full-scale rig, whereas MTR and TRAST are model-scale rigs. The TTR is an isolated rotor rig for measuring performance and loads only, whereas the MTR and TRAST are semispan rotor–wing-pylon rigs that also permit whirl flutter measurements. A major effort is also underway in Europe, led by Royal Netherlands Aerospace Center, to develop an Advanced Testbed for Tiltrotor Aeroelastics in support of a Next-Generation Civil Tiltrotor-Technology Demonstrator [11,12].

There is significant literature on tiltrotor testing, but historically all models had proprietary properties unavailable in the public domain. All the historical tests are compiled in Table 1. Full-scale tiltrotor testing began with the 25-ft-diameter Bell XV-3 rotor in 1957. It was tested at the NASA Ames Full-scale Aerodynamics Complex (NFAC) 40- by 80-ft wind tunnel. Stability of a low-frequency whirl mode was recorded [13]. Next, a 25-ft-diameter rotor, the Bell Model 300, was tested at the NFAC in 1970. This time, a full set of wing beam, chord, and torsion stability data was measured up to 202 kt [14]. A 26-ft-diameter rotor, the Boeing Model 222, was also tested on the same wing as the Model 300 but with a hingeless hub. It was tested at the NFAC in 1972. Beam and chord stability was measured up to 192 kt [15]. This led to the development of the XV-15 aircraft. The 25-ft-diameter XV-15 rotor was also tested at NFAC in 1978, but stability was not measured [16]. The XV-15 led to the military V-22 program and the civilian BA609. The modern NASA TTR is a 26-ft-diameter BA609 rotor. It had its first test in 2018. Performance and loads were measured, but not stability [17].

Small-scale models were also developed and tested over the years for fundamental understanding and analysis validation. These were either models of the same rotors or models of the V-22, which again had proprietary properties. The 1/4.622 scale of the Boeing M222, a 5.5-ft-diameter hingeless rotor, was tested at the Boeing V/STOL wind tunnel in 1976. Stability was not tested [18]. Another 1/9.422 scale model of the Boeing M222, a 2.8-ft-diameter hingeless rotor, and a 1/8.888 scale model of the Bell 300 rotor, also 2.8 ft in diameter, were tested at the MIT Wright Brothers wind tunnel in 1975. This was the first model with an interchangeable hub. The focus was on gust stability and not whirl flutter [19]. Then came the 1/5 scale model tests of the V-22 by Bell/Boeing at the NASA TDT during the 1980s. These tests supported the development of the V-22. Multiple tests were carried out, beginning from 1984. Beam and chord stability up to almost 200 kt was collected [20]. The right-hand rotor and wing of that model later became the Wing and Rotor Aeroelastic Test System (WRATS). It has been tested extensively at the NASA TDT, beginning from 1995. Beam and chord stability were recorded up to 180 kt [21]. Sikorsky developed an interesting 1/6 scale model of the Variable-Diameter Tiltrotor (VDTR) concept, which had an

Received 15 March 2024; accepted for publication 22 September 2024; published online 6 January 2025. 

*Graduate Research Assistant, Department of Aerospace Engineering, Alfred Gessow Rotorcraft Center; aakinwal@umd.edu. Student Member AIAA.

†Associate Professor, Department of Aerospace Engineering, Alfred Gessow Rotorcraft Center; datta@umd.edu. Associate Fellow AIAA.

**Table 1 Historical tiltrotor tests**

| Model | Year | Tunnel | Rotor size | Data |
|---|---|---|---|---|
| Full-scale | | | | |
| XV-3 | 1957 | NFAC | 25-ft | Flutter |
| Model 300 | 1970 | NFAC | 25-ft | B,C,T; Flutter |
| Model 222 | 1972 | NFAC | 26-ft | B,C; Flutter |
| XV-15 | 1978 | NFAC | 25-ft | Loads |
| TTR | 2018 | NFAC | 26-ft | Loads |
| Model-scale | | | | |
| 1/4.622 M222 | 1976 | Boeing V/STOL | 5.5-ft | Loads |
| 1/9.422 M222 | 1975 | MIT | 2.8-ft | Loads |
| 1/8.888 M300 | 1975 | MIT | 2.8-ft | Loads |
| 1/5 V-22 | 1984 | TDT | 7.6-ft | B,C; Flutter |
| WRATS | 1995 | TDT | 7.6-ft | B,C; Flutter |
| 1/6 VDTR | 1990s | UTRC | 8.2-ft hover | Loads |
| — — | — — | — — | 5.4-ft cruise | — — |
| TRAM | 1998, 2000 | DNW, NFAC | 9.5-ft | Loads |
| MTR | 2021 | Navy SWT | 4.75-ft | B,C; Flutter |

Note: B: Beam, C: Chord, T: Torsion.

8.2-ft-diameter rotor in hover, and reduced to 5.4 ft in cruise to reduce tip speed. It was tested at the United Technologies Research Center wind tunnel (UTRC) in the early 1990s. No stability data was available [22]. The Tiltrotor Aeroacoustic Model (TRAM) was a 1/4 Mach scale model of the V-22. It was developed at NASA Ames in the late 1990s and tested at the German-Dtramtch wind tunnel (DNW) in 1998, and again at the NFAC in 2000. However, no stability tests were conducted [23,24]. In summary, these historical tests either did not publish properties of the model or did not provide extensive data. None of the models studied the effect of the gimbal. The model developed and tested, as reported in this paper, tries to bridge some of this gap. Having test data that is easily accessible by the community is crucial for building trust in models and methods, as it enables others to reproduce results and collaborate on verification and validation of test results and models.

The specialty of the MTR is that it is a research rig with interchangeable blades, hubs, and wing spar, and not locked into any particular aircraft. It is anchored, however, to a loosely $f = 1/5.26$ Froude-scale XV-15. The MTR is also capable of installation at multiple facilities. The first whirl flutter tests of the MTR with the present blades were conducted between October 26th and November 2nd, 2021 at the Naval Surface Warfare Center Carderock Division (NSWCCD) 8- by 10-ft large subsonic wind tunnel. That test reached a speed of 100 kt. The test reported in this paper was conducted between August 1st and 5th, 2022 at the University of Maryland 7.75- by 11-ft Glenn L. Martin tunnel (GLMT). This test went deeper into the high-speed domain, reaching 200 kt, which corresponds to a full-scale speed of 458 kt, surpassing almost all turbo-prop aircraft, albeit with low helical Mach numbers. At Froude scale, the Mach number is reduced by the factor $\sqrt{f} = 2.3$ (for same gravity and speed of sound) and therefore remains quite low. Thus, the two tests together provided data over a wide speed range that can be useful for fundamental understanding as well as validation of advanced comprehensive analysis, such as reported in Ref. [25]. The key takeaways of the GLMT test were the following: the first test at the NSWCCD tunnel only went up to 100 kt, but this test extended the range of speeds by 100 kt, obtaining frequency and damping values for the aeroelastic tiltrotor modes, including torsion, which was not measured previously; the damping obtained from the NSWCCD test was extracted only with moving block; the data from the GLMT test was extracted with both moving block and Prony, which added verification to the results, comparing data sets from two different tunnels and comparing two different hub configurations for a larger speed range.

Following this introduction, the first section gives a short overview of the model. The next section describes the fabrication of the Froude-scale carbon fiber blades. The same set of blades were used in both tunnels. They were refurbished and recalibrated for the Glenn Martin tests. The third section describes the signal processing with moving-block and Prony methods. The fourth section presents the results. Finally, conclusions are drawn.

## II. MTR Model

A three-view diagram of the MTR is shown in Fig. 1. The detailed structural and inertial properties were published earlier in Refs. [3–5]. Some key properties are summarized in Table 2.

The rotor radius is 2.375 ft (0.7239 m), which is 1/5.26 scale of the 25-ft-diameter Bell XV-15 rotor tested during the 1970s at the Ames 40- by 80-ft wind tunnel. The blade and spar properties are loosely Froude scaled to that model. The Froude-scaled rpm is 1050, which is 17.5 Hz; so the rotation 1/rev frequency means 17.5 Hz. The hub is gimballed but it can also be locked. The blade lag frequency is a departure from the XV-15 and is very stiff. The torsion frequency was not measured or reported for the XV-15. The wing is 18% thick: thinner than the XV-15 (23%) but thicker than the 40- by 80-ft test wing (13%). The wing-pylon frequencies in /rev are about 0.3/rev in beam, 0.55/rev in chord, and 0.8/rev in torsion. The wing torsion is softer than the Ames 40- by 80-ft model (1.36/rev), the XV-15 (1.07/rev), and the V-22 aircraft (1.04/rev). This is due to the slip ring and load cell masses on the pylon. These masses also shifted the pylon center of gravity (c.g.) 0.23 ft (0.07 m, 9.7% rotor radius) behind the wing elastic axis, unlike the XV-15, where it is ahead. Therefore, the deviations from the XV-15 are the following: stiffer blade lag, heavier pylon mass, and pylon c.g. located slightly behind the wing elastic axis.

The wing-pylon beam, chord, and torsion frequencies and corresponding damping were measured after installation through impulse testing. The gimbal was locked for these tests. The frequencies measured at the Carderock test were 5.06, 9.65, and 14.4 Hz in beam, chord, and torsion, respectively. The frequencies did not change significantly. They were 5.1, 9.48, and 14.65 Hz at GLMT. The damping measured at Carderock was 0.4, 0.57, and 2%. The damping measured at GLMT was 0.48, 1.3, and 1.15%. Therefore, the chord damping doubled and torsion almost halved. These values are necessary for analysts.

## III. Blade Fabrication

The proprotor blades were fabricated in-house. High twist makes the blades special relative to typical helicopter blades. Fabrication requires a twisted mold, and procedures unique to its geometry, such as twisted foam cuts and insertion of leading-edge weights. The fabrication steps follow a procedure established and validated recently in Refs. [26,27]. It consists of multiple steps as described next. The blade uniform properties correspond to the main outboard portion of the XV-15 blades. The twist is a linear $-37$ deg. The airfoil is VR-7. Blades have a span of 21 in and a constant chord of 3.15 in. Blade cross-sectional makeup is shown in Fig. 2.

The blades consist of a foam core, a root insert, leading-edge weights, a spar, and skin. The foam is Rohacell IG-31. The root insert is cut from Aluminum 6061, with dimensions of $2.5 \times 1 \times 1$ in. Seven leading-edge weights are used; they are made from tungsten carbide and are each 2.5 in long with a 9/64-in diameter. The carbon fiber is a prepreg IM712/8552, donated by Boeing. It is a bidirectional weave of $\pm 45$ deg. The spar and skin both use the same layup. The adhesive film used to adhere the foam to the carbon fiber is Hysol PL7000, which is an epoxy film adhesive that has a curing temperature of 350°F.

The blade fabrication process begins by cutting a piece of foam slightly longer than the chord. The foam span is 21 in and the chord 3.25 in. The foam chord is slightly longer than the blade chord, so that the foam remains secured in place inside the blade mold during curing.

After the foam is placed in the mold, bolts, nuts, and washers are used to clamp the top and bottom halves together. To achieve even clamp pressure, the bolts are tightened in a star pattern, beginning at the outer corners and working inward. The mold is cured in an oven at 375°F for 1.5 h.

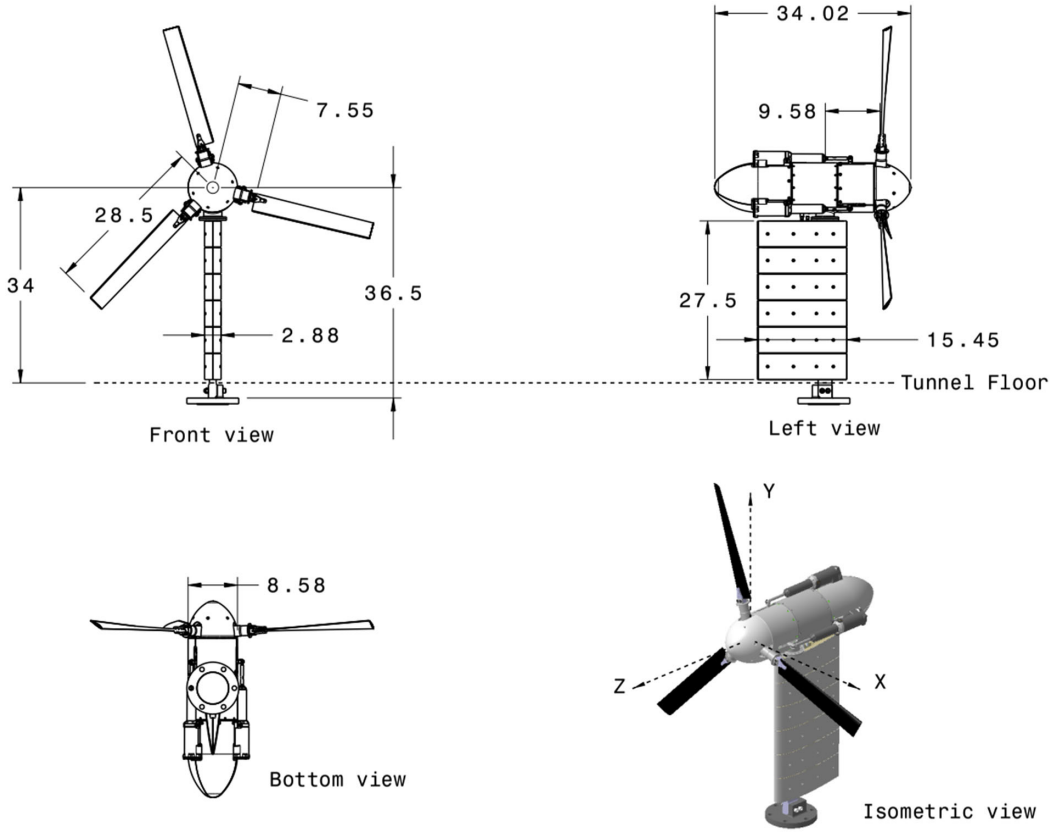


**Fig. 1 Three-view diagram of the Maryland tiltrotor rig; dimensions in inches.**

**Table 2 MTR overview**

| | | |
|---|---|---|
| Rotor properties | | |
| Radius R | ft | 2.375 |
| Rotor speed | rpm | 1050 |
| Hub | — — | Gimbaled |
| $\delta_3$ | deg | −15 |
| Flap $\nu_\beta$ coll | /rev | 1.79 |
| Flap $\nu_\beta$ cyclic | /rev | 1.05 |
| Lag $\nu_\zeta$ | /rev | 5.08 |
| Wing-pylon properties | | |
| Wing airfoil | — — | NACA 0018 |
| Pylon c.g. | — — | −0.097 R |
| Beam $\omega_b$ | Hz | 5.1 |
| Chord $\omega_c$ | Hz | 9.48 |
| Torsion $\omega_t$ | Hz | 14.65 |
| Beam $\zeta_b$ | % critical | 0.48 |
| Chord $\zeta_c$ | % critical | 1.3 |
| Torsion $\zeta_t$ | % critical | 1.15 |

Note: /rev is nondimensional frequency scaled by rotor speed.

The mold is removed from the oven, and left to cool overnight. The bolts are removed in the same star pattern as they were applied. Once the foam is removed from the mold, any excess material is cut to the proper length. About 1/8 in should be trimmed from the trailing edge to facilitate the connection of the carbon fiber skin from the upper and lower surfaces.

The root insert pieces are machined in a four-axis Computer Numerical Control (CNC) milling machine. A CATIA v5 model of the root insert is imported into a SprutCam software. The software generates a G-code, which defines the cutting path of the mill. The G-code is uploaded into the CNC machine. A 3/8-in steel-ball mill bit is used to machine the part. For the root insert holes a 3/16-in steel drill bit is used. The holes are for bolts that connect the blade grips to the blades.

The foam core is cut into a leading-edge and a trailing-edge piece. To prepare the spar, the leading-edge piece is wrapped separately. There needs to be enough space for two plies of carbon fiber to be wrapped around the leading-edge piece, and this is taken into account when measuring the thickness of the foam.

Because the cured foam core is highly twisted, a three-dimensional (3-D)-printed part is custom built to untwist a section of the blade while it is milled. This 3-D-printed part is secured to a vice. The mill is halted once it surpasses the length of the part, and the part moved further along the core and milling is continued. A 1/16-in aluminum mill bit is used to cut the foam core.

The slots for the root insert and leading-edge weights are also milled with special care due to the twist. The root insert is positioned on the top of the leading-edge foam, where it will be placed, and its outline is traced using an X-ACTO knife. The root insert is traced with an X-ACTO knife and cut at an angle to accommodate the twist. The leading-edge and trailing-edge foam pieces with the root insert are shown in Fig. 3. The leading-edge foam is again clamped to another 3-D-printed part for the leading-edge slots to be cut. There are seven slots cut, which are distributed evenly along the length of the leading edge.

The leading-edge weights are wrapped in one layer of adhesive and inserted into the milled slots. The root insert is also wrapped in one layer of adhesive and placed in its slot. Another layer of adhesive is put around both the leading-edge and trailing-edge pieces. The adhesive is cut longer than the foam to account for the twist.

Two carbon fiber plies are cut for the blade skin and for the spar. The ply is cut at $\pm 45$ deg using a right triangle tool. The ply is cut longer than the blade length to account for the high twist. The excess material on each side ensures that the carbon fiber plies perfectly cover the entire surface area.

The leading-edge piece wrapped twice in carbon fiber forms the spar. The fiber is wrapped in such a way that it is not stretched but still pulled tight. The plies should be cut precisely so that there are exactly two plies of material around the spar.

In order for the plies from the top and bottom to overlap at the trailing edge, the skin is started 1/8 in behind the trailing edge. The fabric must be laid following the twisted shape of the blade.

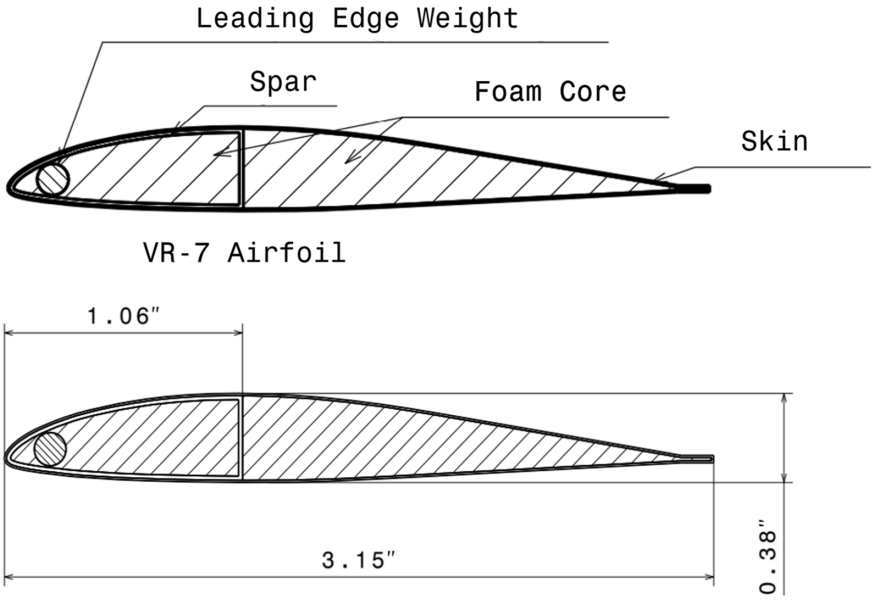


**Fig. 2 Blade cross section.**

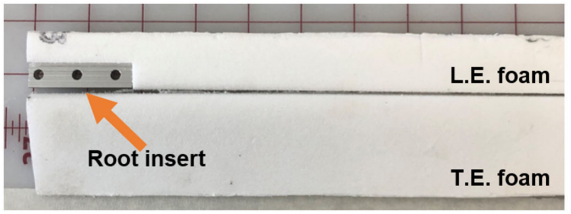


**Fig. 3 Foam pieces with root insert.**

**Table 3 Measured properties of fabricated blades**

| | Full blade weight (grams) | C.G. (% of chord) |
|---|---|---|
| Blade 1 | 164.39 | 26.55% |
| Blade 2 | 163.39 | 26.9% |
| Blade 3 | 165.85 | 29.38% |

Once the spar and trailing-edge pieces are wrapped, they are ready to be cured. To prevent the carbon fiber from sticking to the blade mold, a release ply is wrapped around the blade. The same mold used earlier to cure the foam is used again. The blade is cured for 2.5 h at 375°F and is left overnight to cool.

The excess material on the trailing edge and leading edge is shaved off using a Dremel. The final trimming is performed using sand paper until the trailing- and leading edges are perfectly straight with the correct dimensions. The finished product is shown in Fig. 4.

Four blades were fabricated; the three identical ones were selected for testing. The mass and c.g. properties are shown in Table 3. The maximum deviation in mass is 1.5%. The c.g. is behind the quarter-chord, unlike the CAD. For the heaviest blade, the c.g. is 4.3% c behind the quarter-chord. The stiffness properties were the following: $EI_N = 20.1\ N-m^2$ in normal bending, $EI_C = 937\ N-m^2$ in chordwise bending, and $GJ = 62\ N-m^2$ in torsion.

## IV. Wind-Tunnel Testing

The GLMT has a test section 7.75 ft high and 11.04 ft wide. Maximum speed is 200 kt, which translates to Mach 0.3 for sea-level conditions. The sphere test turbulence factor is 1.05 and measured hot wire intensity is 0.21%. The floor boundary layer has a displacement thickness of about 0.125 in at the center of the test section. The MTR baseplate is mounted to a specially fabricated interfacing post. Figure 5 shows the MTR being installed and tested in the wind tunnel. The interfacing post as well as the wing internal structure can also be seen. For information on the NSWCCD tunnel and test, refer to Ref. [3].

After installation, the first step is to perform an impulse test on the model to measure structural damping values. They are typically needed by analysts. Next, the model is powered on for blade tracking and balance. The blades were tracked and balanced near zero collective $\theta_{75}$. After track and balance, the model is ready for stability testing.

The collective $\theta_{75}$ is set to 60 deg and the tunnel is turned on. Then, the collective is reduced slowly. The rotor starts turning faster and faster. The cyclics are trimmed to achieve zero gimbal flapping. Once the target rpm is achieved, perturbations are introduced to excite wing beam, chord, and torsion modes. Three trials were performed per mode. The blade pitch is excited in the rotating frame through the electric actuators in the fixed frame. The type of pitch excitation (collective, longitudinal, or lateral cyclic), magnitude, frequency, and the number of cycles are specified. A longitudinal cyclic $\theta_{1s}$ of approximately 0.5-deg input at a frequency of 5 Hz perturbs the model in beam; a collective $\theta_{75}$ of approximately 0.5 deg at 9.5 Hz

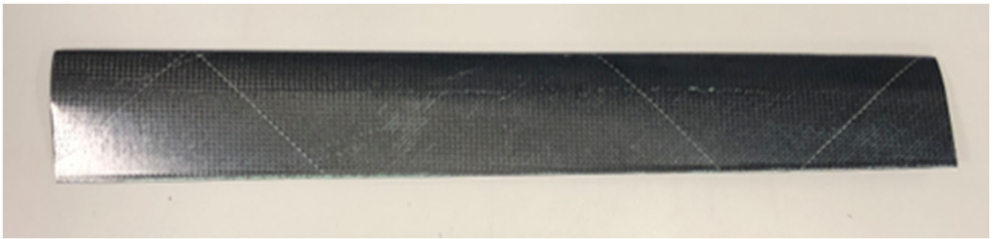

**Fig. 4 Model blade.**

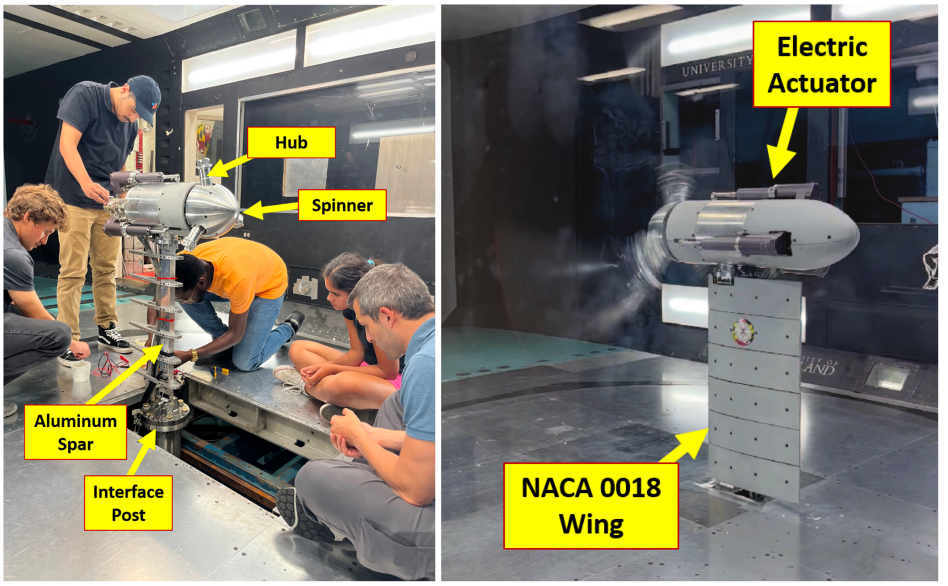


a) Installation on the interface post b) Testing at 200 knots

**Fig. 5 Model installed at the Glenn L. Martin tunnel.**



perturbs in chord, and lateral cyclic $\theta_{1c}$ of approximately 2 deg at 14.5 Hz perturbs in torsion. The strain at the root on the wing spar is recorded. There are a total of six strain gauges on the wing spar: two for beam, two for chord, and three for torsion. Figure 5b shows the MTR in the tunnel during an active test.

## V. Signal Processing

Two methods are used to extract damping from these signals: 1) moving block, and 2) Prony. The procedures are summarized next.

Figure 6 shows typical wing strains in response to beam, chord, and torsion excitation. It is clear that the torsion response is the most difficult to extract, as it is the weakest in magnitude and also the fastest to decay.

### A. Moving-Block Method

The moving-block method approximates the damped frequency to be equal to the natural frequency, and is therefore applicable for damping typically less than 5% critical. It is quite effective for noisy signals. For more in-depth information on the moving-block method, refer to Refs. [28,29]. The general procedure is illustrated using a beam mode signal.

Consider the beam mode signal at 190 kt shown in Fig. 7. Figure 7a shows the signal. A 3-s decay from the end of the perturbation is selected for damping extraction. There are 3000 samples in 3 s of data. A Fast Fourier Transform (FFT) is taken to find frequency of decay. The signal is divided into smaller blocks. Each block represents a box car or a rectangular window. This is shown in Fig. 7b. Three block sizes were used: 512, 1024, and 2048.

An FFT is performed on each block. This is shown in Fig. 7c. Then the block is shifted by one step and FFT is performed again. This process is repeated until the block has traversed the entire decaying portion of the signal. The peak amplitude of the frequency of interest is stored from the FFT. For the beam mode, this frequency is 5 Hz, which can be seen in Fig. 7c. This is repeated for each block. A natural logarithm of the amplitude is taken and is plotted vs the starting time of each moving block. An oscillating signal that decreases with time is the result. A least-squares regression line is fitted over this oscillating signal and the slope is set to $-\zeta\omega_n$, where $\zeta$ is the damping ratio and $\omega_n$ is the natural frequency. For small damping ratios, this frequency can be assumed to equal the damped frequency obtained from FFT earlier. Thus, $\zeta$ is obtained. What is plotted in results is $\zeta \times 100$ as the percent damping. The process can be repeated for various block sizes, as shown in Fig. 7d.

### B. Prony Method

The Prony method is similar to Fourier but decomposes a signal into damped sinusoids instead of sinusoids. Refer to Ref. [30] for general information on Prony. To apply Prony, first the decaying portion of the signal is selected. Next $N$ equidistant samples are selected. The Prony method assumes that a linear relationship exists between consecutive samples. For example, $M$ samples are related to the $(M+1)^{\text{th}}$ sample through $M$ coefficients, $p_0, p_1, \ldots, p_{M-1}$. Applying this to the first $M+1$ samples would give Eq. (1).

$$x_1 p_0 + x_2 p_1 + x_3 p_2 + \cdots + x_M p_{M-1} = x_{M+1} \tag{1}$$

The assumption is valid for any signal produced by a system governed by an underlying set of differential equations. Applying the relation from the last $M+1$ samples to the first $M+1$ samples produces $N-M$ equations.

$$\begin{bmatrix} x_{N-M} & x_{N-M+1} & x_{N-M+2} & \cdots & x_{N-1} \\ x_{N-M-1} & x_{N-M} & x_{N-M+1} & \cdots & x_{N-2} \\ x_{N-M-2} & x_{N-M-1} & x_{N-M} & \cdots & x_{N-3} \\ \vdots & \vdots & \vdots & & \vdots \\ x_2 & x_3 & x_4 & \cdots & x_{M-1} \\ x_1 & x_2 & x_3 & \cdots & x_M \end{bmatrix} \begin{pmatrix} p_0 \\ p_1 \\ p_2 \\ \vdots \\ p_{M-1} \end{pmatrix} = \begin{pmatrix} x_N \\ x_{N-1} \\ x_{N-2} \\ \vdots \\ x_M \\ x_{M+1} \end{pmatrix} \tag{2}$$

This relation is of the form $\boldsymbol{A}\boldsymbol{p} = \boldsymbol{x}$, where $\boldsymbol{x}$ is the observation vector containing the samples, and $\boldsymbol{A}$ is a Toeplitz matrix. Note that applying the relation from the first $M+1$ samples to the last $M+1$ samples would produce the same $N-M$ equations, but arranged in reverse order, so that $\boldsymbol{A}$ would be a Hankel matrix.

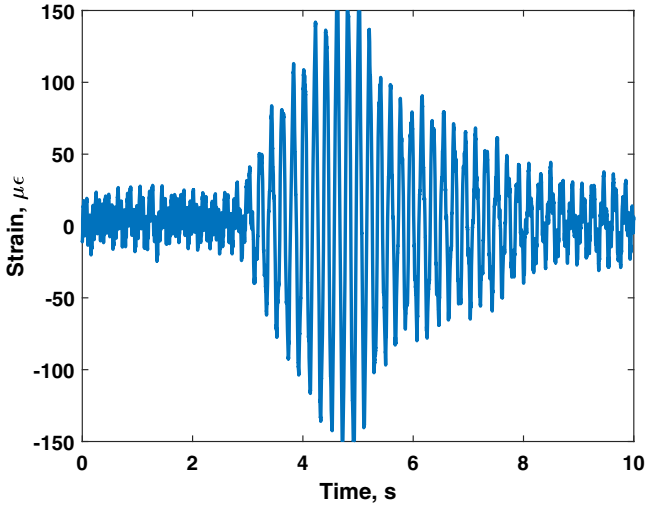


a) Beam response from a 5-Hz longitudinal cyclic excitation

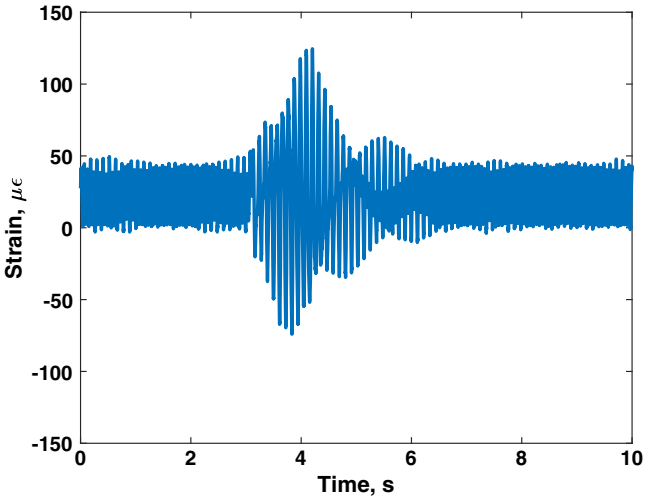


b) Chord response from a 9.5-Hz collective excitation

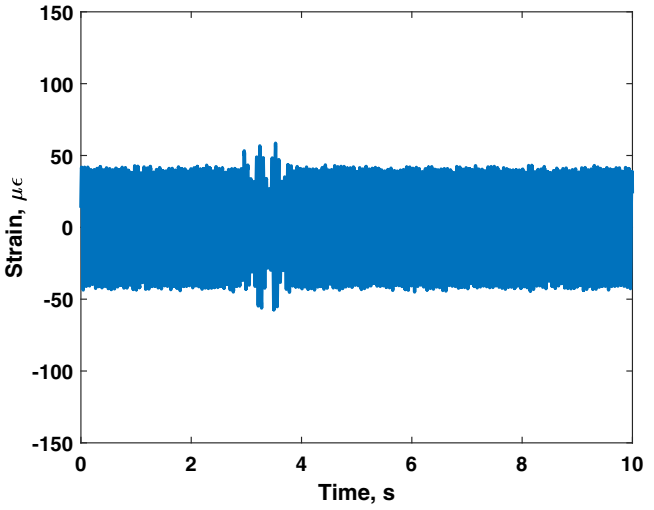


c) Torsion response from a 14.5-Hz lateral cyclic excitation

**Fig. 6 Flutter excitation of wing modes at 110 kt.**

Regardless, the solution produces the coefficients vector $\boldsymbol{p} = [p_0, p_1, \ldots, p_{M-1}]$. In theory, only $M$ equations should suffice to calculate the $M$ coefficients. In practice, due to noise in the experimental signal, more than $M$ equations are needed and the least-squares solution is taken. These coefficients are used to form a polynomial:

$$P_0 + P_1 x + P_2 x^2 + \cdots + P_{M-1} x^{M-1} - x^M = 0 \qquad (3)$$

The roots of this polynomial are $e^{s\Delta t}$, where $s = -\zeta\omega_n \pm i\omega_n\sqrt{1-\zeta^2}$ are the stability roots, and $\omega_n$ and $\zeta$ are the natural frequency and damping ratio, respectively. Prony is preferred for motions with higher damping, such as torsion.

### C. Signal Processing for Torsion

The torsion mode proved very difficult to excite at many tunnel speeds. When it could be excited, extracting damping from the raw strain signal required careful processing. Figure 8 illustrates the processing for a 110-kt gimbal-locked trial.

Figure 8a shows the raw strain signal. Clearly, the perturbation response is so weak that applying either moving block or Prony will not provide a sensible damping value. An FFT of the strain signal shown in Fig. 8b provides clarity. Torsion is excited but a large 1/rev frequency (17.5 Hz) from rotor imbalance, higher in magnitude to the 0.75/rev torsion frequency (14 Hz), hides the signal.

This 1/rev can be attributed to residual hub imbalance after track and balance. A notch filter was applied to the raw strain signal to remove the 1/rev. The notch filter is a bidirectional Infinite Impuse Response (IIR) filter suggested by our colleague Dr. Abhishek Shastry. It was used to surgically remove the 1/rev and all integer harmonics up to 8/rev. The bidirectionality of the filter ensures no phase delay is introduced. It also means that the full signal should be available. Thus, it is applicable as a postprocessing tool but not for online extraction during testing. After applying this filter, as shown in Fig. 8c, only torsion remains in the FFT (the strain signal is now clean with a discernible perturbation and decay, as shown in Fig. 8d) and the moving-block and Prony methods can now be applied on the decay to calculate damping.

## VI. Collective vs Speed

The rotor was tested in free-wheeling mode. The collective $\theta_{75}$ was trimmed to obtain 1050 rpm. Below 30 kt there was no collective setting that would turn the rotor at 1050 rpm, as there was not enough energy in the flow.

Figure 9 shows the collective reading from the two different tests conducted at the Navy Carderock and Glenn L. Martin tunnels. The Navy Carderock data was only up to 100 kt. There is good agreement in the data from the two tunnels. This provided confidence that the model maintained the same aerodynamic characteristics.

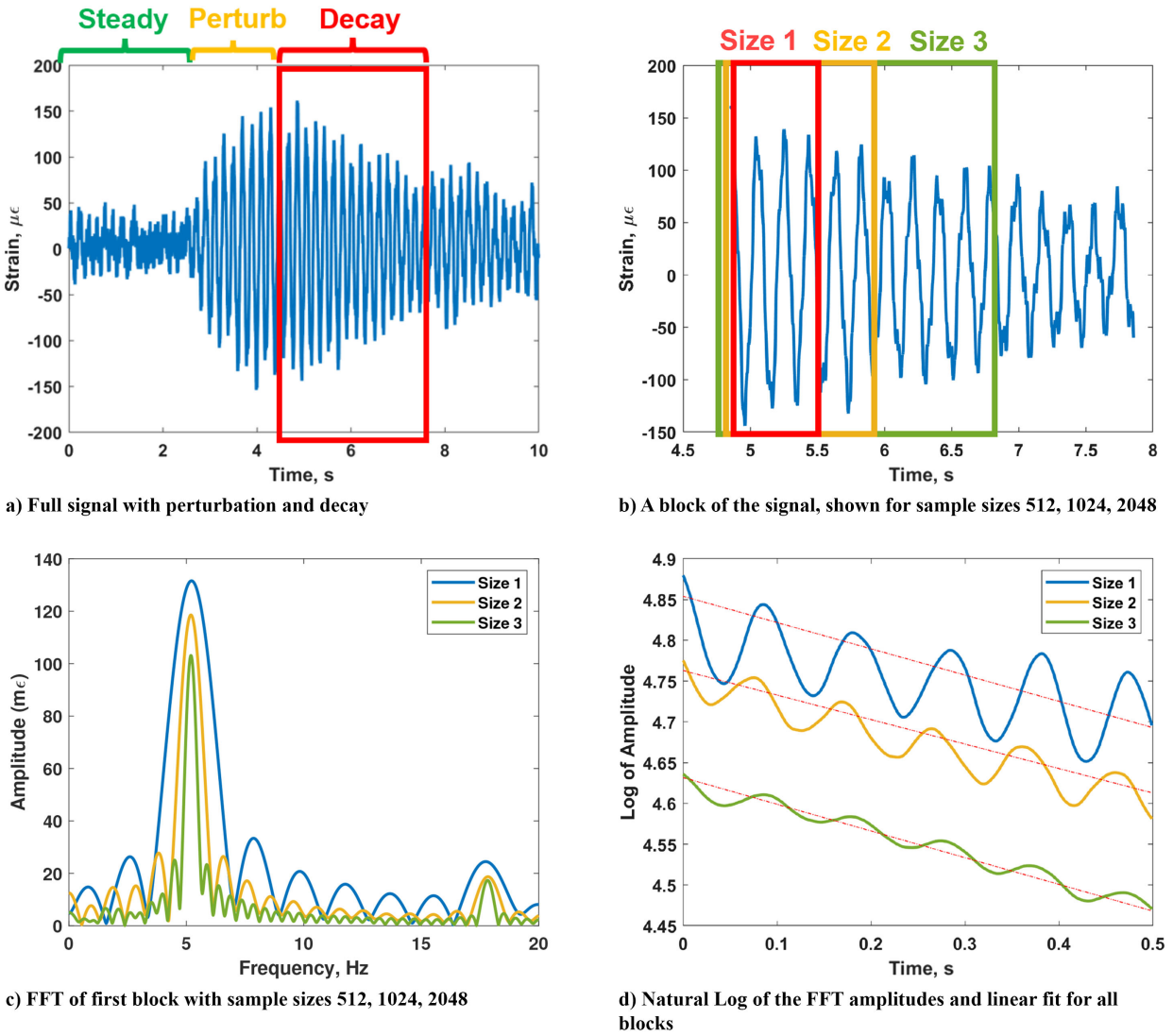


a) Full signal with perturbation and decay

b) A block of the signal, shown for sample sizes 512, 1024, 2048

c) FFT of first block with sample sizes 512, 1024, 2048

d) Natural Log of the FFT amplitudes and linear fit for all blocks

**Fig. 7 Moving-block method illustrated on a beam signal at 190 kt; block sizes of 512, 1024, and 2048 samples corresponding to 0.512, 1.024, and 2.048 s.**

Figure 10 shows the collective for Blades 2 and 3 at the Glenn Martin tunnel. The collectives are nearly equal up to 150 kt, after which they differ by 4 deg. This is likely an encoder error on Blade 3, as the rig showed no sudden vibrations from loss in tracking. The pitch encoder of Blade 1 stopped working during the test so it could not be confirmed whether Blade 1 matched Blade 2.

Figure 11 compares the collective angles of the gimbal-free and gimbal-locked configurations. The results are from Blade 2. Generally they are the same, as expected, because under steady axial flow the blades always see a locked hub. Gimbal locked has slightly higher collective than gimbal free, from 30 to 145 kt.

## VII. Frequencies

The wing-pylon frequencies are shown in Fig. 12 for the gimbal-free configuration. The frequencies did not change appreciably for the various parameters examined hereafter so they are not repeated. Torsion is shown for a limited speed range. Torsion was difficult to excite, and so data could be successfully measured only between 80 and 122 kt.

## VIII. Damping

The baseline configuration consists of straight blades and is gimbal free. Figure 13a shows the damping of the beam mode extracted using the moving-block method.

Damping begins slightly below 1% at 30 kt, then increases to 2% at 193 kt. There is not much scatter in the data up to 100 kt, but is quite significant above 150 kt. Three trials were taken at each speed, all of which are plotted in order to document the error band. In regard to the scatter at high speed, beam is the lowest frequency mode, so it is more susceptible to disturbances in the flow. We believe the type of actuation input plays a role as well. Beam was excited with cyclic, whereas chord was excited with collective. Collective generally has less noise.

Figure 13b shows the damping of the chord mode extracted using the moving-block method. The beam mode is also shown. Damping begins at around 1.5%, and is relatively constant as tunnel speed is increased. It then increases to 2% around 100 kt, but drops to 1% starting from around 170 kt. The drop is marked from 170 to 193 kt. There is much less scatter between each trial compared to the beam mode.

Figure 13c shows the damping of the torsion mode extracted using the moving-block method. The beam and chord modes are also shown for comparison. Torsion damping could be successfully measured only between 80 and 122 kt. At other speeds torsion proved difficult to excite. Damping begins at around 3% at 80 kt. There is what appears to be a peak of about 4.8% at 110 kt. There is significant scatter among the three trials at most speeds. The assumption inherent in moving-block that the damped frequency is close to the natural frequency ($\omega \approx \omega_n \sqrt{1-\zeta^2}$) may not be valid because torsion damping is higher. So, Prony is explored next.

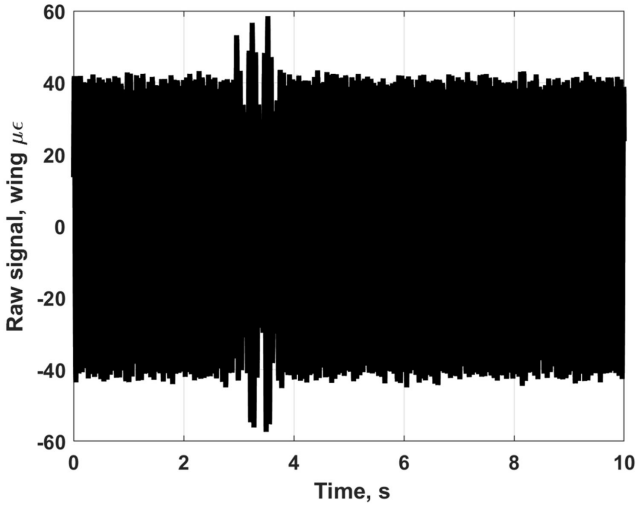


a) Strain signal

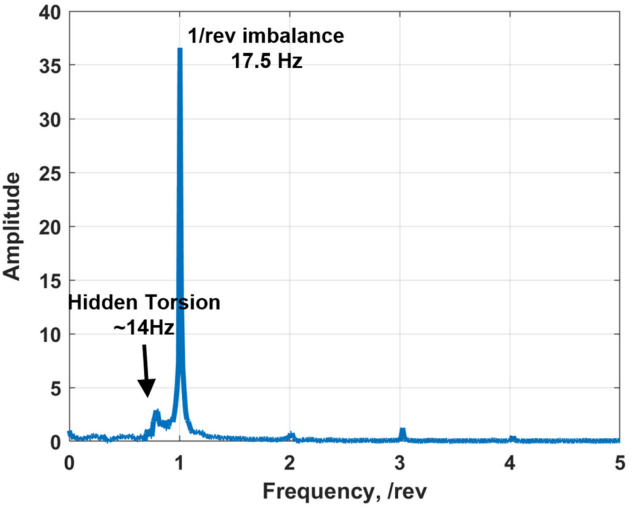


b) Strain signal with decay highlighted

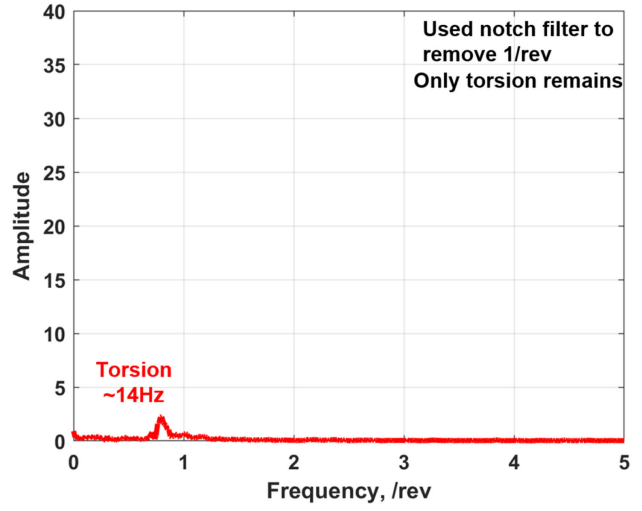


c) Decaying portion of signal

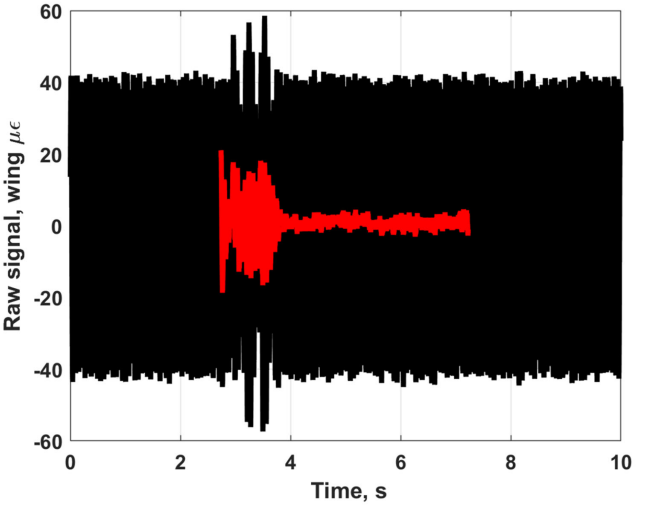


d) Filtered strain signal

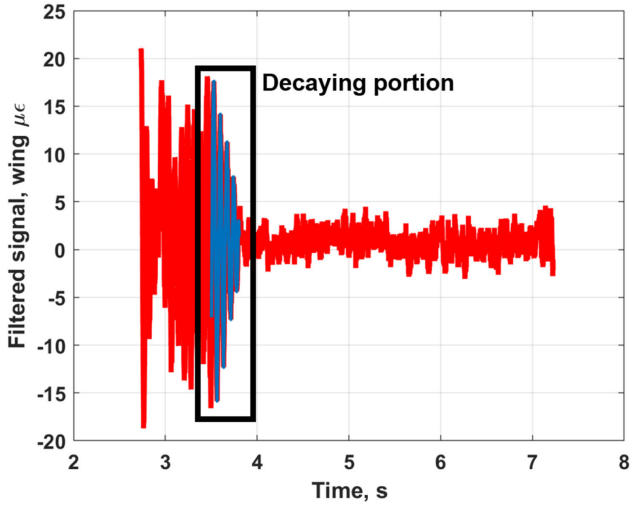


e) Strain signal with decay highlighted

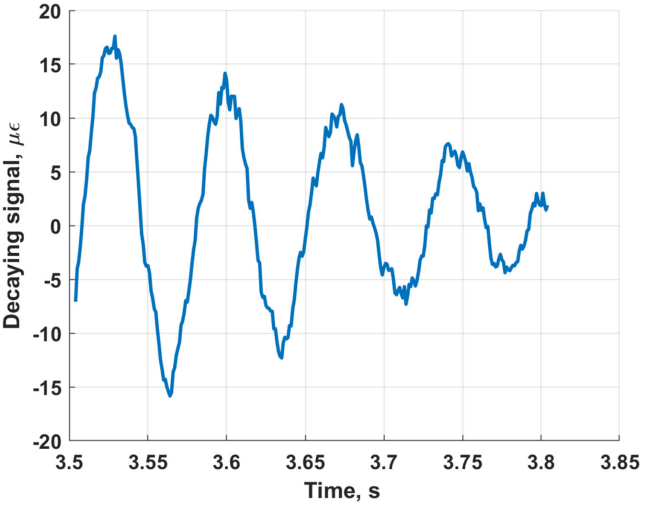


f) Decaying portion of signal

**Fig. 8 Filtered 110-kt torsion signal; bidirectional IIR filter extracts torsion response from raw signal.**

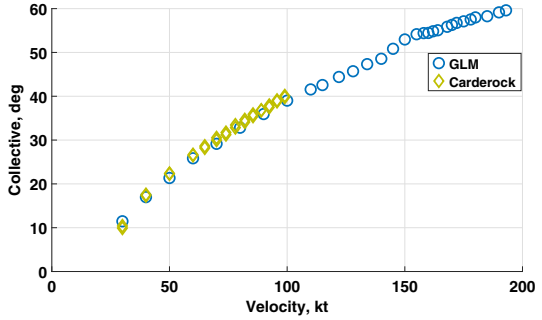


Fig. 9 Collective vs speed; Navy Carderock and Glenn Martin tunnels.

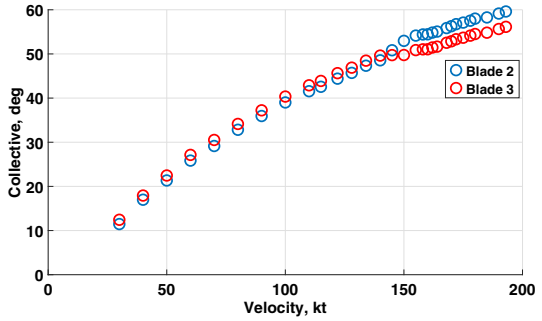


Fig. 10 Collective vs speed; Blades 2 and 3.

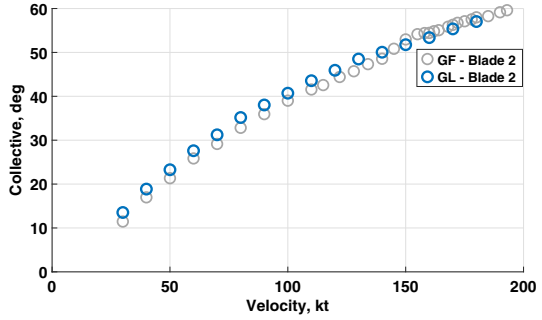


Fig. 11 Collective vs speed; gimbal free vs gimbal locked.

## IX. Moving-Block vs Prony

The Prony method was applied to compare whether one method was more effective than the other in reducing the scatter in data. Another reason was to cross verify the extracted damping.

Figure 14a shows beam damping from moving-block compared to Prony. The damping values are almost identical until 130 kt, after which there are slight differences. The trend remains the same. The amount of scatter between trials is not much different.

Figure 14b shows chord damping from moving-block compared to Prony. Chord results are also almost identical. The relatively sharp drop from 170 to 193 kt is confirmed by both.

Prony is particularly important in torsion because of high damping. Figure 14c shows torsion damping from moving-block compared to Prony. Although the magnitude of the values remains the same between the two methods, no clear trend can be revealed. The scatter between trials is still significant. Because the scatter in Prony is comparable to moving-block, the mathematical scatter caused by the moving-block assumption is not the cause. The scatter could be attributed to the perturbations being excited with cyclic, which tends to have some noise.

## X. Carderock vs Glenn L. Martin

There was a unique opportunity to compare test data from two different tunnels for exactly the same model and identical blades. Figure 15 shows the frequency data from both tests for the baseline configuration. Similarly, Fig. 16 shows the damping data from both tests for the baseline configuration. The data from the Navy Tunnel was only up to 100 kt so the comparison is only up to that same speed. The general trend in damping is the same for beam although there seems to be less scatter in the Glenn Martin tunnel. The chord is similar in trend but the magnitudes are slightly different. Scatter is low in both tunnels up to 100 kt, indicating that the scatter is from the model and not the tunnel. Overall the data indicates that the experiments are repeatable and the data is reliable.

## XI. Gimbal Free vs Gimbal Locked

The gimbal is now locked. Locking the gimbal is a special feature of the MTR that generates a stiff-in-plane hingeless hub. When the gimbal is locked, the flapping frequencies are higher. Locking the gimbal introduces hub moments that are expected to impact chord

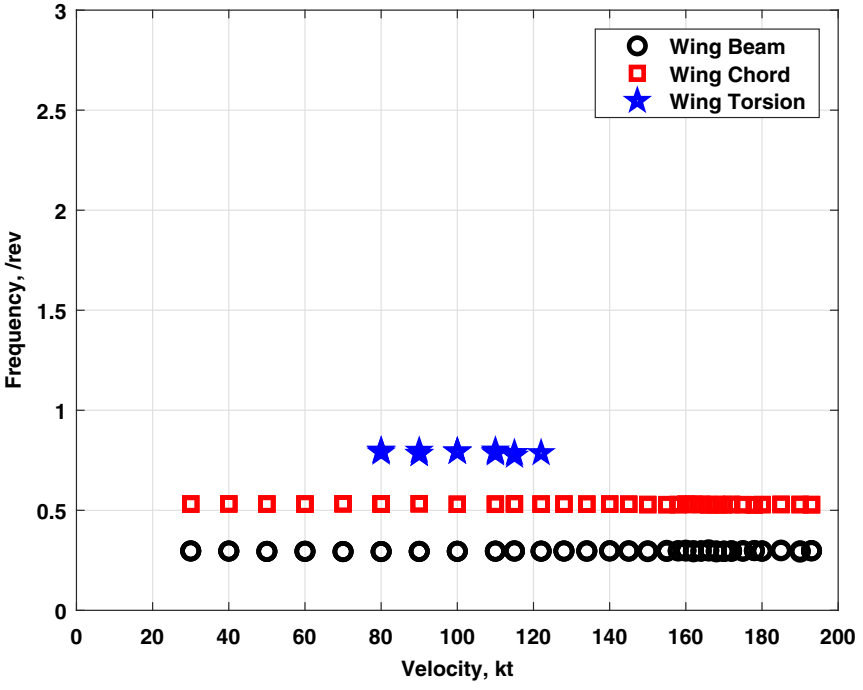


Fig. 12 Frequency vs speed.

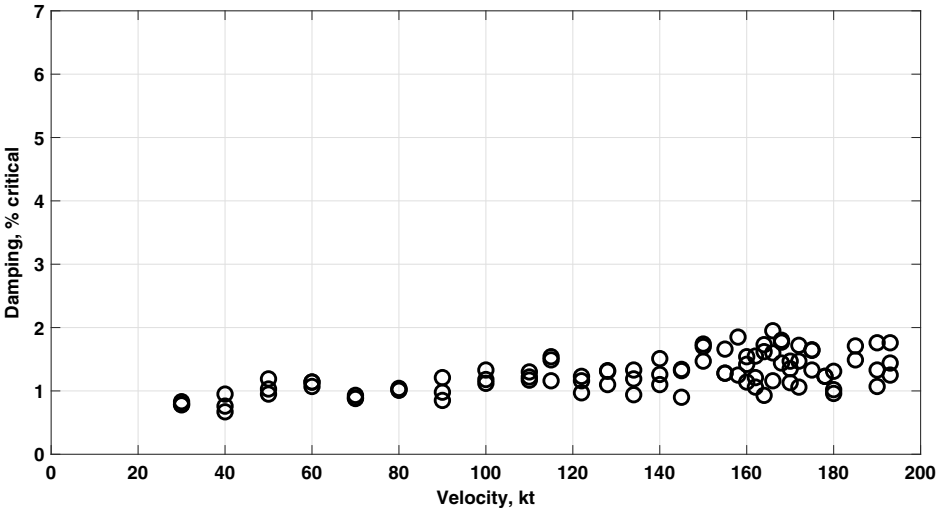


a) Beamwise damping vs tunnel speed

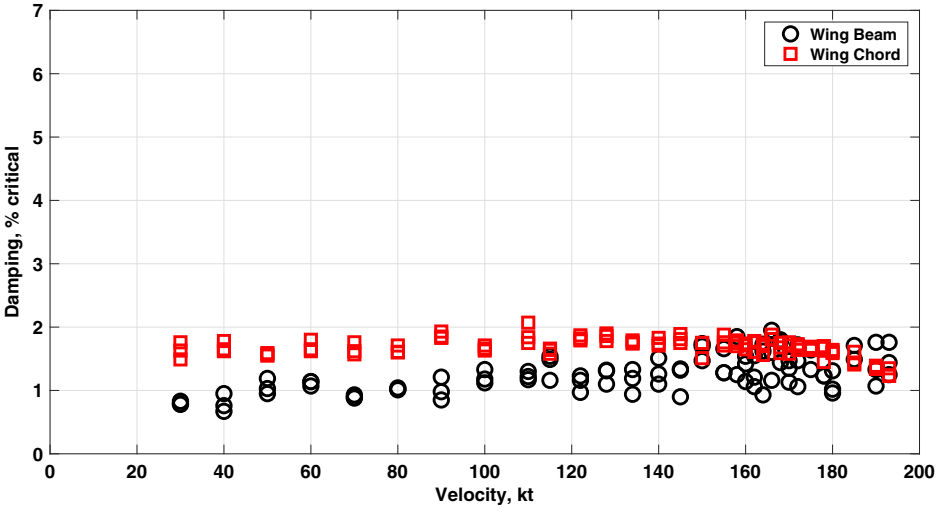


b) Beam and chord damping vs tunnel speed

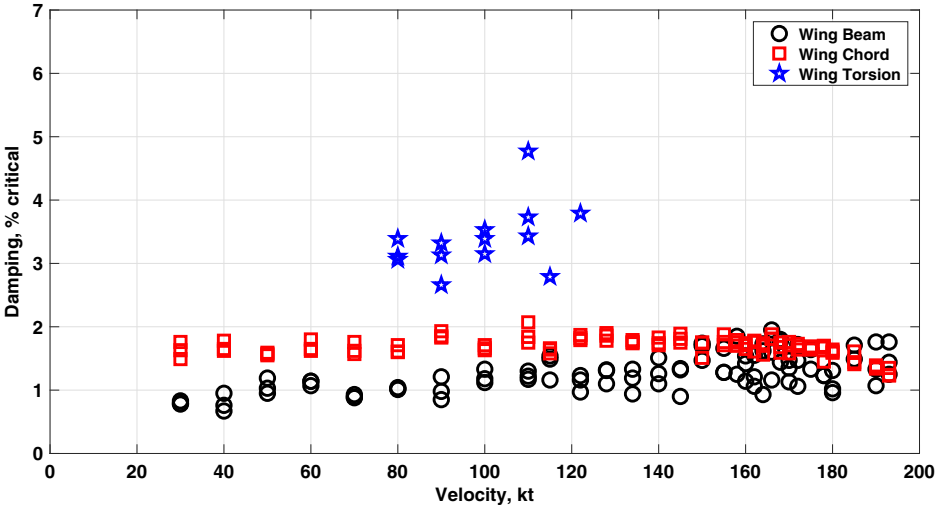


c) Beam, chord, and torsion damping vs tunnel speed

**Fig. 13 Damping vs speed for the baseline gimbal-free configuration.**

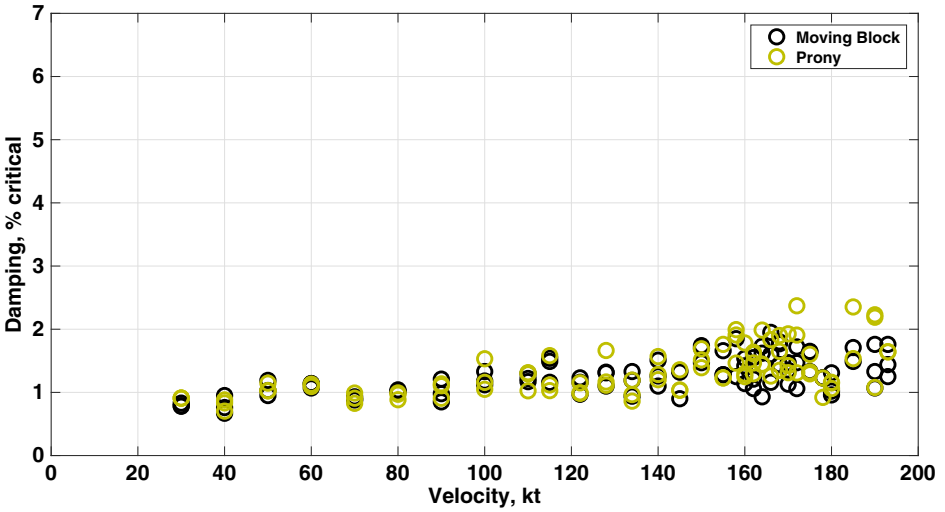


a) Beamwise damping vs tunnel speed

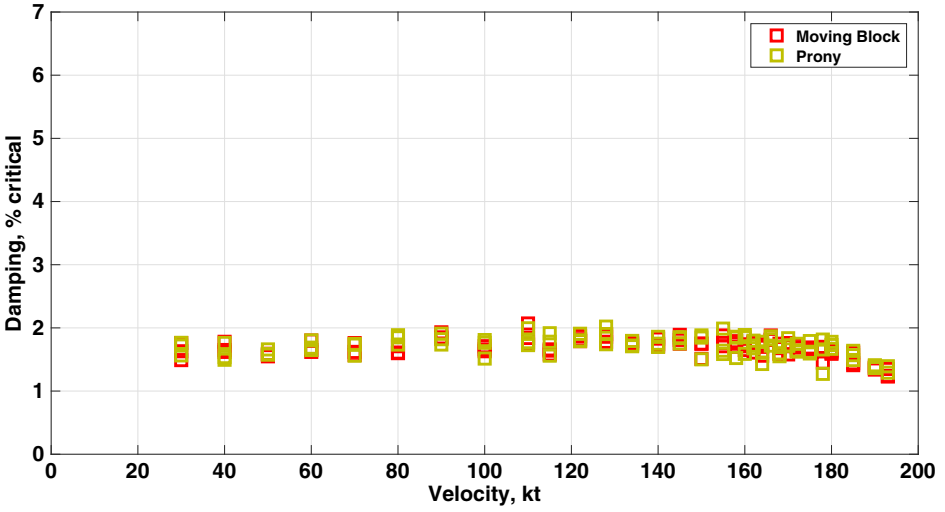


b) Chordwise damping vs tunnel speed

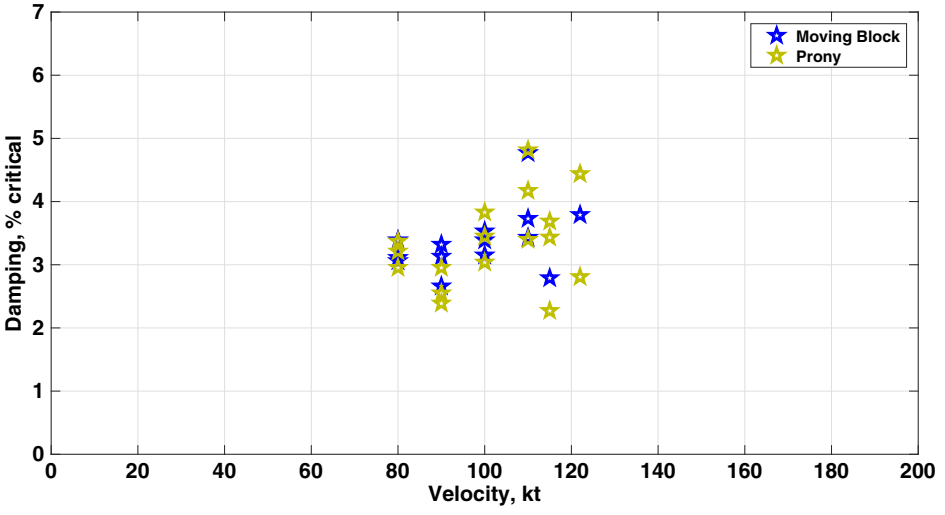


c) Torsion damping vs tunnel speed

**Fig. 14 Moving block vs Prony.**

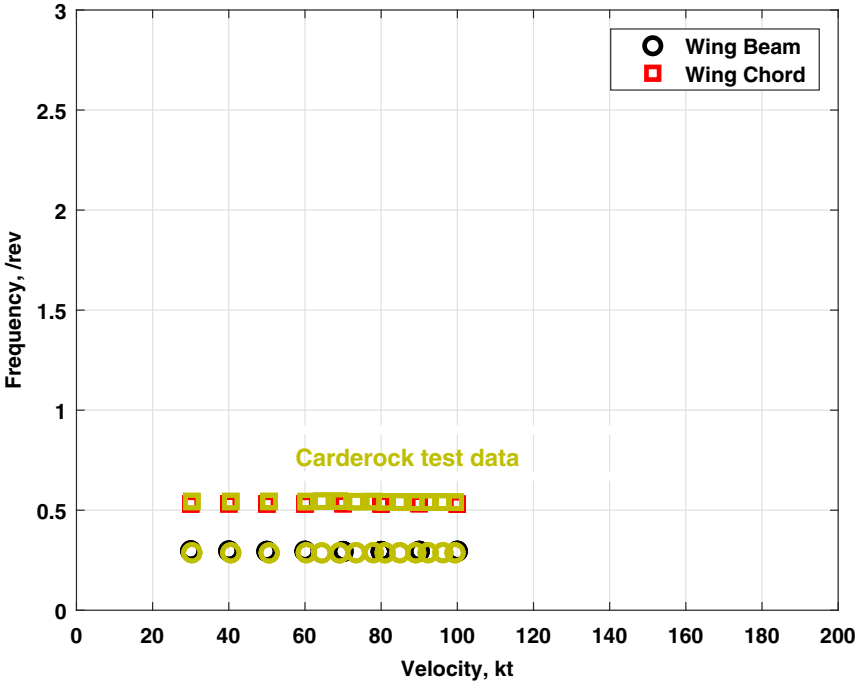


**Fig. 15 Frequency vs speed; comparison of data from two wind tunnels.**



through pitch moment and torsion through roll moment. The pitch and roll moments are about the $y$ and $x$ axes respectively, as shown in Fig. 1.

For illustrating the effect on the MTR frequencies, the predicted fan plot is shown in Fig. 17. A gimballed hub has both articulated (also called cyclic) and hingeless (also called collective) frequencies. These are marked as "Art." and "Hng." in the figure. The first three articulated frequencies at 1050 rpm are 1.11/rev (Art. Flap 1), 2.3/rev (Art. Flap 2), and 4.72/rev (Art. Flap 3). The first three hingless frequencies at 1050 rpm are 1.71/rev (Hng. Flap 1), 4.66/rev (Lag 1), and 7.23/rev (Hng. Flap 2). The limited test data shown is from Ref. [27].

Figure 18a shows beam damping for the gimbal-locked and gimbal-free configurations. The beam mode damping did not change much and followed the same trend of increasing with speed. There is, however, a difference in the amount of scatter between trials. Both configurations have low scatter below 120 kt. The gimballed hub scatter increases with speed. The gimbal-locked data appear visually to have less scatter, but are fewer data points. Also, naturally for gimbal locked, there is less flapping motion, so there is a smaller source of variation in perturbations.

Figure 18b shows chord damping. Locking the gimbal increases damping significantly. Damping starts higher around 3% at 30 kt, and has a decreasing trend. It meets the gimbal-free value around 160 kt, after which both appear to show a decreasing trend. When the gimbal is locked, it introduces perturbation roll moment $M_x$ (or yaw moment in airplane nomenclature), which affects the chord mode through the lateral flapping ($\dot{\beta}_{1c}$) term and pitch motion velocity ($\dot{\alpha}_y$).

Figure 18c shows torsion damping. The increase in damping is now even more significant. The trend is also reversed from baseline. The moment introduced when the gimbal is locked is pitching moment $M_y$, which affects torsion through the longitudinal flapping ($\dot{\beta}_{1s}$) term and roll motion velocity ($\dot{\alpha}_x$) term. There is significant scatter in some trials, particularly at 80 and 110 kt, which makes discerning the trends somewhat difficult. The 7% damping at 80 kt appears to be an anomaly. All values were doubled checked for consistency using Prony.

In summary, chord and torsion are distinctly different between gimbal free and locked. When the gimbal is locked, damping increases significantly and also presents a distinctly different trend with speed for torsion.

## XII. Conclusions

A 4.75-ft-diameter Froude-scale proprotor was tested on the Maryland Tiltrotor Rig in two different wind tunnels. Aeroelastic stability data was acquired at the Navy Carderock tunnel and the Glenn L. Martin wind tunnel, with two hub conditions: gimbal free (baseline) and gimbal locked (stiff-in-plane hingeless). The data consisted of frequency and damping of beam, chord, and torsion motions of the rotor–wing-pylon system at a Froude-scale rpm of 1050. The roots were extracted with moving-block and Prony methods and compared. Based on this work, the following key conclusions were drawn:

1) The beam and chord damping remained low, around 1–2%. For the baseline gimballed configuration, wing beam damping began around 1% and increased to 2% at 193 kt. Chord damping began around 1.5% and remained constant until 100 kt, where it reached 2%, then dropped to around 1% between 170 and 193 kt.

2) Torsion damping was higher, around 3–6%. Torsion began at around 3%, followed by a peak at around 100 kt. Thus, torsion was the most highly damped, followed by chord, then beam. Torsion was also the most difficult to excite and showed maximum scatter.

3) The gimbal-locked condition increased chord and torsion significantly, to almost twice that of the gimballed hub, and also changed their trends with speed. Chord damping began at 3% then dropped to gimballed values around 160 kt. Torsion damping began at 6% and remained higher than gimballed throughout.

4) The model remained flutter-free up to 200 kt, and although the chord damping showed signs of a sudden drop after 175 kt. The 200-kt speed achieved corresponded to a 458-kt speed of a full-scale aircraft, albeit with low-tip Mach number.

5) Moving-block and Prony are equally effective methods for extracting test data. Damping extracted using Prony was in close agreement with moving block. Torsion damping was the most difficult to measure. A special processing technique using a bidirectional Infinite Impulse Response filter was used to extract the decaying signal.

6) The Glenn L. Martin tunnel test significantly expanded the Naval Surface Warfare Center Carderock Division (NSWCCD) test by the following: speed increasing from 100 to 200 kt; measuring torsion, which was not measured in the prior NSWCDD test;

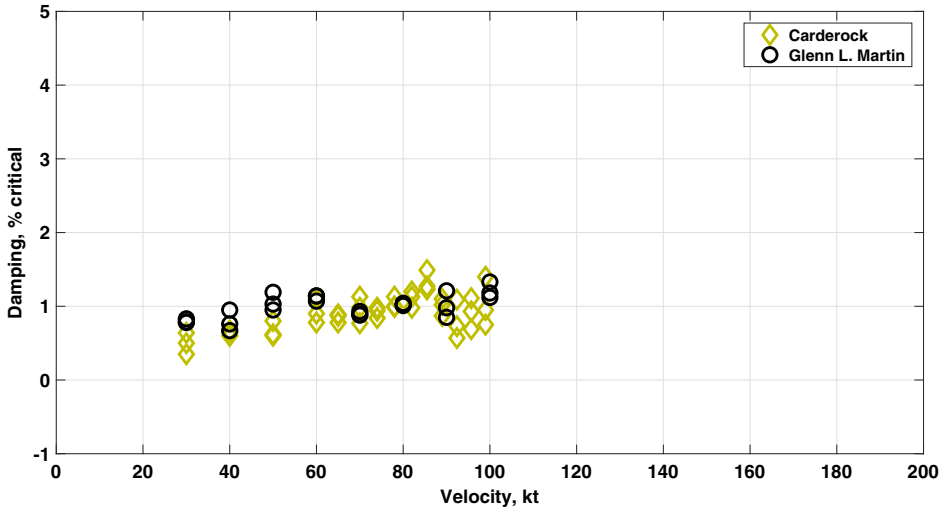


a) Beamwise damping vs tunnel speed

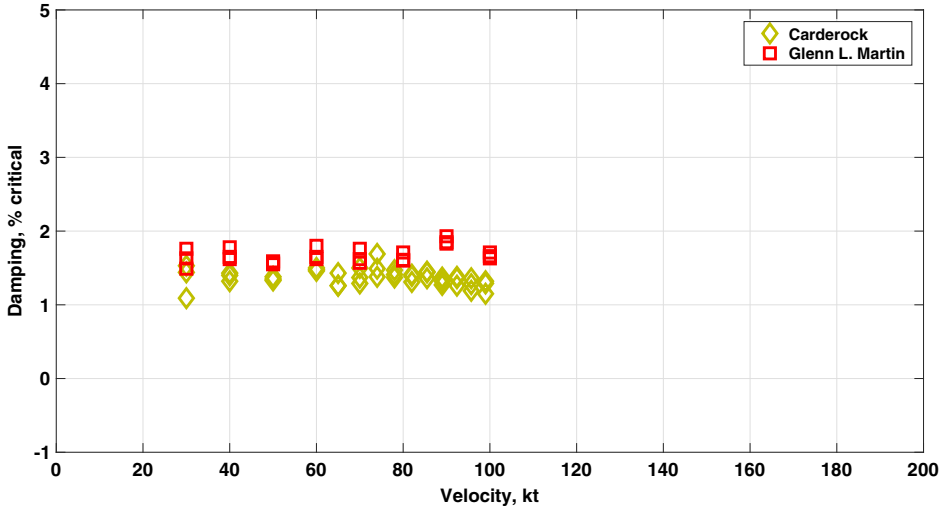


b) Chordwise damping vs tunnel speed

**Fig. 16 Comparison of data from two wind tunnels; only beam and chord were measured in Carderock tests.**

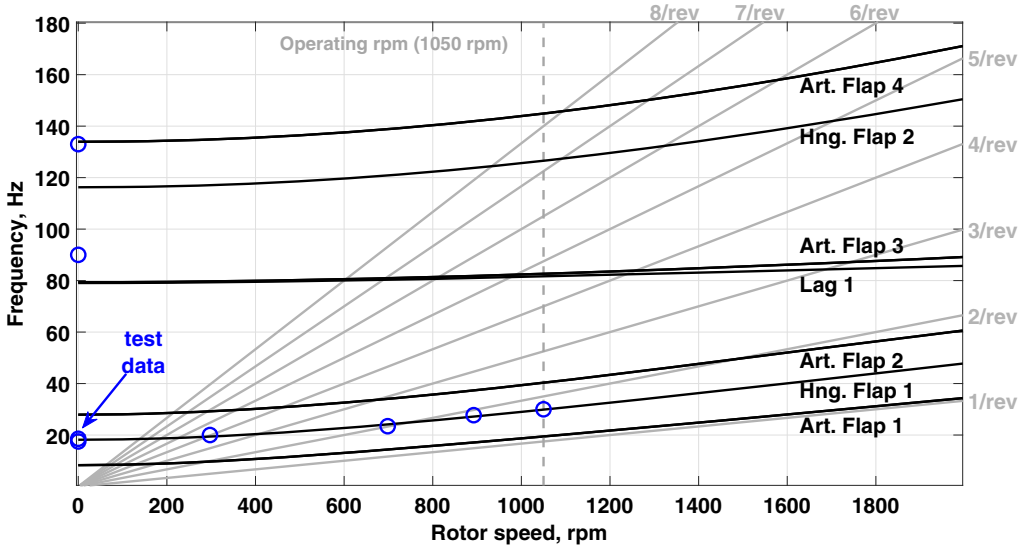


**Fig. 17 MTR fanplot.**

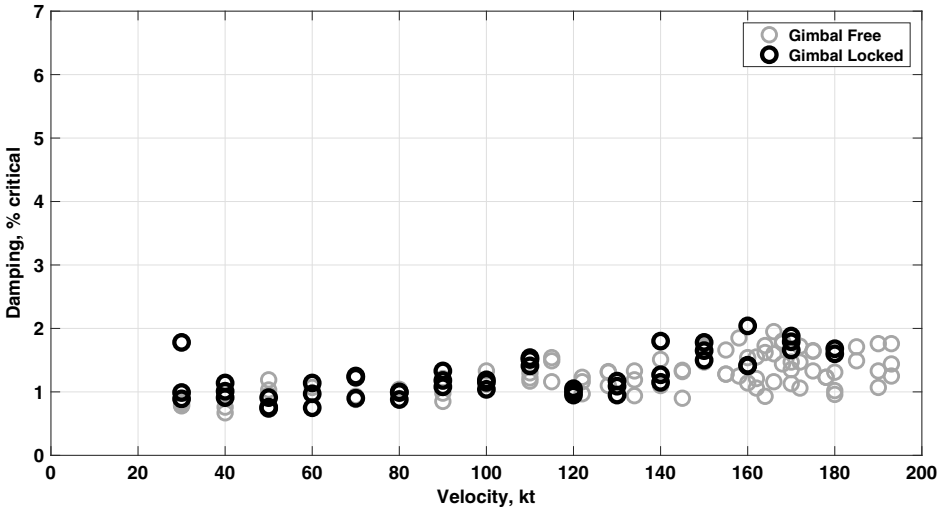


a) Beamwise damping vs tunnel speed

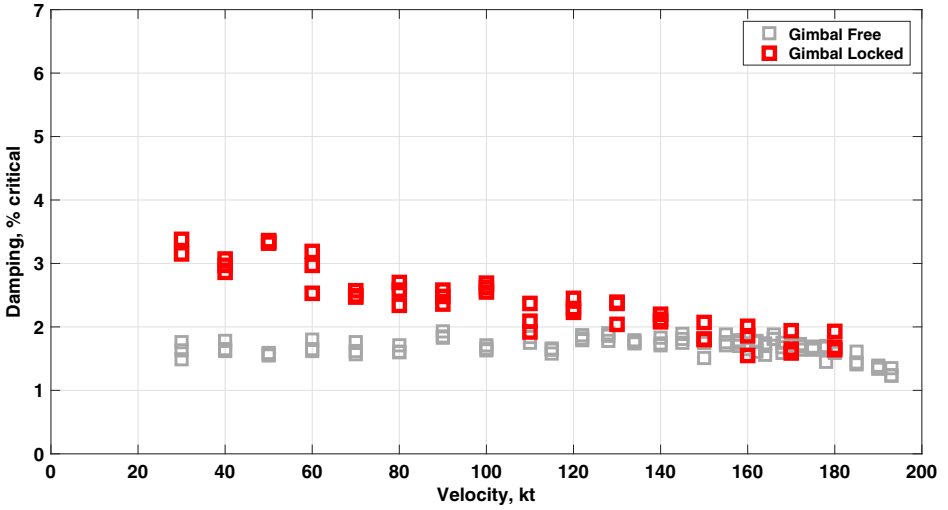


b) Chordwise damping vs tunnel speed

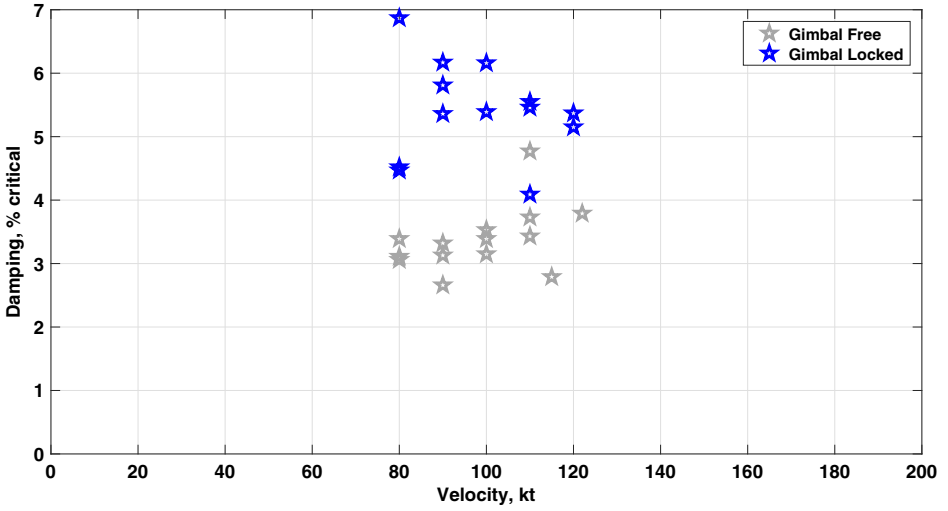


c) Torsion damping vs tunnel speed

**Fig. 18 Comparison of hub types; gimbal free vs gimbal locked.**

extracting damping with both moving-block and Prony; and being able to compare data from two different wind tunnels.

## Acknowledgments

This work was carried out at the Alfred Gessow Rotorcraft Center, University of Maryland at College Park, under the Army/Navy/NASA Vertical Lift Research Center of Excellence (VLRCOE) (grant number W911W62120003) with technical monitoring from Mahendra Bhagwat. We wish to thank Seyhan Gul and Hyeonsoo Yeo of the U.S. Army, and Wayne Johnson of NASA for useful suggestions.

## References

[1] Acree, C. W., Sheikman, A., and Norman, T., "High-Speed Wind Tunnel Tests of a Full-Scale Proprotor on the Tiltrotor Test Rig," *VFS 75th Annual Forum & Technology Display*, May 2019. https://doi.org/10.4050/F-0075-2019-14736

[2] Acree, C. W., "Vertical Climb Testing of a Full-Scale Proprotor on the Tiltrotor Test Rig," *VFS Aeromechanics for Advanced Vertical Flight Technical Meeting*, NASA ARC-E-DAA-TN76769, Jan. 2020.

[3] Tsai, F., Sutherland, J., Akinwale, A., Morin, A., Gul, S., and Datta, A., "Development and Whirl Flutter Test of the Maryland Tiltrotor Rig," *Journal of the American Helicopter Society*, Vol. 69, No. 1, Jan. 2024, pp. 1–15. https://doi.org/10.4050/JAHS.69.012009

[4] Sutherland, J., Tsai, F., and Datta, A., "Whirl Flutter Test of Swept-Tip Tiltrotor Blades," *Journal of the American Helicopter Society*, Vol. 69, No. 1, Jan. 2024, pp. 1–12. https://doi.org/10.4050/JAHS.69.012010

[5] Gul, S., and Datta, A., "Prediction and Validation of Whirl Flutter Data of the Maryland Tiltrotor Rig," *Journal of the American Helicopter Society*, Vol. 69, No. 1, Jan. 2024, pp. 1–11. https://doi.org/10.4050/JAHS.69.012011

[6] Tsai, F., Sutherland, J. R., Akinwale, A., Morin, A., Gul, S., and Datta, A., "Whirl Flutter Test of the Maryland Tiltrotor Rig: Overview," *SciTech Forum,* AIAA Paper 2022-0567, Jan. 2022.

[7] Sutherland, J., Tsai, F., and Datta, A., "Whirl Flutter Test of the Maryland Tiltrotor Rig: Swept-Tip Blades," *SciTech Forum,* AIAA Paper 2022-0568 Jan. 2022.

[8] Gul, S., and Datta, A., "Whirl Flutter Test of the Maryland Tiltrotor Rig: Prediction and Validation," *SciTech Forum*, AIAA Paper 2022-0927, Jan. 2022.

[9] Kreshock, A. R., Thornburgh, R., and Wilbur, M., "Overview of the Tiltrotor Aeroelastic Stability Testbed," *SCITECH Forum*, AIAA Paper 2022-0566, Jan. 2022.

[10] Yeo, H., Kang, H., and Kreshock, A. R., "Unified Modeling of the TiltRotor Aeroelastic Stability Testbed for Proprotor Whirl Flutter," *Journal of Aircraft*, Vol. 60, No. 3, May 2023, pp. 857–869. https://doi.org/10.2514/1.C036950

[11] Cocco, A., Masarati, P., van t Hoff, S., and Timmerman, B., "Tiltrotor Whirl Flutter Analysis in Support of NGCTR Aeroelastic Wind Tunnel Model Design," *Proceedings of the47th European Rotorcraft Forum*, Paper 93, Glasgow, U.K., Sept. 2021, pp. 7–10.

[12] van't Hoff, S., van Vilsteren, J., Cocco, A., and Pierangelo, M., "Design of a Tiltrotor Semi-Span Wind Tunnel Model for Whirl Flutter Investigations," *SCITECH Forum*, AIAA Paper 2023-1306, Jan. 2023.

[13] Koenig, D. G., and Morelli, J. P., "Full-Scale Prop-Rotor Stability Tests on the XV3 at High Advance Ratios," NASA TM-2015-218812, 2015.

[14] Anon, "Advancement of Proprotor Technology. Task II: Wind-Tunnel Test Results," Bell Helicopter Company, NASA-CR-114363, Sept. 1971.

[15] Magee, J. P., and Alexander, H. R., "Wind Tunnel Tests of a Full Scale Hingeless Prop/Rotor Designed for the Boeing Model 222 Tilt Rotor Aircraft," Boeing Vertol Company, NASA CR-114664, Oct. 1973.

[16] Weiberg, J. A., and Maisel, M. D., "Wind-Tunnel Tests of the XV-15 Tilt Rotor Aircraft," NASA-TM-81177, April 1980.

[17] Kottapalli, S., and Acree, C. W., Jr., "Correlation of Full-Scale Isolated Proprotor Performance and Loads," *Vertical Flight Society 75th Annual Forum & Technology Display*, May 2019. https://doi.org/10.4050/F-0075-2019-14568

[18] Magee, J. P., and Alexander, H. R., "Wind Tunnel Test on a 1/4.622 Froude Scale, Hingeless Rotor, Tilt Rotor Model, Volumes I-IV," NASA CR-151936-151939, Sept. 1976.

[19] Ham, N. D., Bauer, P. H., Lawrence, T. H., and Yasue, M., "A Study of Gust and Control Response of Model Rotor-Propellers in a Wind Tunnel Airstream," NASA-CR-137756, Aug. 1975.

[20] Popelka, D., Sheffler, M., and Bilger, J., "Correlation of Test and Analysis for the 1/5-Scale V-22 Aeroelastic Model," *Journal of the American Helicopter Society*, Vol. 32, No. 2, April 1987, pp. 21–33. https://doi.org/10.4050/JAHS.32.21

[21] Piatak, D. J., Kvaternik, R. G., Nixon, M. W., Langston, C. W., Singleton, J. D., Bennett, R. L., and Brown, R. K., "A Parametric Investigation of Whirl-Flutter Stability on the WRATS Tiltrotor Model," *Journal of the American Helicopter Society*, Vol. 47, No. 2, April 2002, pp. 134–144. https://doi.org/10.4050/JAHS.47.134

[22] Matuska, D., Dale, A., and Lorber, P., "Wind Tunnel Test of a Variable-Diameter Tiltrotor (VDTR) Model," NASA-CR-177629, Jan. 1994.

[23] Johnson, W., "Calculation of Tilt Rotor Aeroacoustic Model (TRAM DNW) Performance, Airloads, and Structural Loads," *American Helicopter Society Aeromechanics Specialists' Meeting*, Nov. 2000.

[24] McCluer, M. S., and Johnson, J. L., "Full-Span Tiltrotor Aeroacoustic Model (FS TRAM) Overview and Initial Testing," *American Helicopter Society Aerodynamics, Acoustics, and Test and Evaluation Technical Specialists' Meeting*, Jan. 2002.

[25] Gul, S., and Yeo, H., "High-Speed Stability Predictions of Maryland Tiltrotor Rig and Parametric Study," *Journal of Aircraft*, Vol. 61, No. 4, July 2024, pp. 1283–1292. https://doi.org/10.2514/1.C037807

[26] Chi, C., Datta, A., Chopra, I., and Chen, R., "Three-Dimensional Strains on Twisted and Swept Composite Rotor Blades in Vacuum," *Journal of Aircraft*, Vol. 58, No. 1, Jan. 2021, pp. 1–16. https://doi.org/10.2514/1.C035746

[27] Sutherland, J., and Datta, A., "Fabrication, Testing, and 3D Comprehensive Analysis of Swept-Tip Tiltrotor Blades," *Journal of the American Helicopter Society*, Vol. 68, No. 1, Jan. 2023, pp. 1–18. https://doi.org/10.4050/JAHS.68.012002

[28] Hammond, C. E., and Doggett, R. V., Jr., "Determination of Subcritical Damping by Moving-Block/Randomdec Applications," *NASA Symposium on Flutter Testing Techniques*, NASA SP-415, Oct. 1975, pp. 59–76.

[29] Bousman, W., and Winkler, D., "Application on the Moving-Block Analysis," *Dynamics Specialists Conference, Structures, Structural Dynamics, and Materials and Co-Located Conferences*, AIAA Paper 1981-0653, April 1981.

[30] Hauer, J. F., Demeure, C. J., and Scarf, L. L., "Initial Results in Prony Analysis of Power System Response Signals," *IEEE Transactions on Power Systems*, Vol. 5, No. 1, Feb. 1990, pp. 80–89. https://doi.org/10.1109/59.49090

I. Chopra
*Associate Editor*